

See discussions, stats, and author profiles for this publication at: <https://www.researchgate.net/publication/23964809>

# ChemInform Abstract: Flexible Polar Nanowires of Cs<sub>5</sub>BiP<sub>4</sub>Se<sub>12</sub> from Weak Interactions Between Coordination Complexes: Strong Nonlinear Optical Second Harmonic Generation

ARTICLE in JOURNAL OF THE AMERICAN CHEMICAL SOCIETY · FEBRUARY 2009

Impact Factor: 12.11 · DOI: 10.1021/ja808242g · Source: PubMed

CITATIONS

53

READS

34

6 AUTHORS, INCLUDING:



In Chung

Northwestern University

41 PUBLICATIONS 1,232 CITATIONS

SEE PROFILE



Joon I. Jang

Binghamton University

70 PUBLICATIONS 1,038 CITATIONS

SEE PROFILE

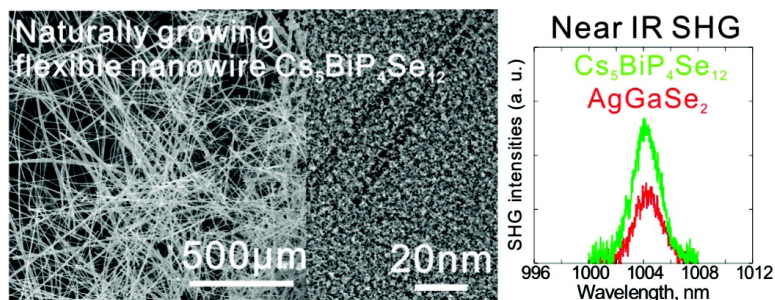
Article

# Flexible Polar Nanowires of CsBiPSe from Weak Interactions between Coordination Complexes: Strong Nonlinear Optical Second Harmonic Generation

In Chung, Jung-Hwan Song, Joon I. Jang, Arthur J. Freeman, John B. Ketterson, and Mercuri G. Kanatzidis

*J. Am. Chem. Soc.*, **2009**, 131 (7), 2647-2656 • DOI: 10.1021/ja808242g • Publication Date (Web): 30 January 2009

Downloaded from <http://pubs.acs.org> on March 4, 2009



## More About This Article

Additional resources and features associated with this article are available within the HTML version:

- Supporting Information
- Access to high resolution figures
- Links to articles and content related to this article
- Copyright permission to reproduce figures and/or text from this article

[View the Full Text HTML](#)

### Flexible Polar Nanowires of Cs<sub>5</sub>BiP<sub>4</sub>Se<sub>12</sub> from Weak Interactions between Coordination Complexes: Strong Nonlinear Optical Second Harmonic Generation

In Chung,<sup>†,‡</sup> Jung-Hwan Song,<sup>§</sup> Joon I. Jang,<sup>§</sup> Arthur J. Freeman,<sup>§</sup> John B. Ketterson,<sup>§</sup> and Mercouri G. Kanatzidis<sup>\*,†,‡</sup>

Department of Chemistry, Michigan State University, East Lansing, Michigan 48824, and Department of Chemistry and Department of Physics and Astronomy, Northwestern University, Evanston, Illinois 60208

Received October 20, 2008; E-mail: m-kanatzidis@northwestern.edu

**Abstract:** The Cs<sub>5</sub>BiP<sub>4</sub>Se<sub>12</sub> salt grows naturally as nanowires that crystallize in the polar space group *Pmc*2<sub>1</sub>, with *a* = 7.5357(2) Å, *b* = 13.7783(6) Å, *c* = 28.0807(8) Å, and *Z* = 4 at 293(2) K. The compound features octahedral [Bi(P<sub>2</sub>Se<sub>6</sub>)<sub>2</sub>]<sup>5−</sup> coordination complexes that stack via weak intermolecular Se···Se interactions to form long, flexible fibers and nanowires. The Cs<sub>5</sub>BiP<sub>4</sub>Se<sub>12</sub> fibers are transparent in the near- and mid-IR ranges and were found to exhibit a nonlinear optical second harmonic generation response at 1 μm that is approximately twice that of the benchmark material AgGaSe<sub>2</sub>. The material has a nearly direct band gap of 1.85 eV and melts congruently at 590 °C. Ab initio electronic structure calculations performed with the full-potential linearized augmented plane wave (FLAPW) method show that the band gap increases from its local density approximation (LDA) spin–orbit coupling value of 1.15 eV to the higher value of 2.0 eV when the screened-exchange LDA method is invoked and explain how the long nanowire nature of Cs<sub>5</sub>BiP<sub>4</sub>Se<sub>12</sub> emerges.

#### 1. Introduction

The synthesis of one-dimensional (1D) inorganic nanostructures, such as nanowires and nanotubes, has attracted great interest because of their promising new optical and electronic properties that can be useful in technological applications.<sup>1,2</sup> Synthetic efforts to create inorganic nanowires and nanotubes involve either the exploration of new compounds with nanofeatures or downsizing existing materials to the nanoscale. Examples of the former include SbPS<sub>4</sub>,<sup>3</sup> and examples of the latter include metals (Au,<sup>4</sup> Ag,<sup>5</sup> Ni,<sup>6</sup> Co, Cu,<sup>7</sup> Bi<sup>8</sup>), oxides (ZnO,<sup>9</sup>

SiO<sub>2</sub>,<sup>10</sup> TiO<sub>2</sub>,<sup>11</sup> V<sub>2</sub>O<sub>5</sub>,<sup>12</sup>), metal chalcogenide binaries [MQ<sub>2</sub> (M = group 4–6 metals,<sup>13</sup> Re,<sup>14</sup> Q = S, Se, Te), Bi<sub>2</sub>S<sub>3</sub>,<sup>15</sup>], nitrides (BN,<sup>16</sup> GaN<sup>17</sup>), and carbides (BC,<sup>18</sup> SiC<sup>19</sup>). The synthetic procedures used to obtain 1D nanostructures, however, can be challenging and generally require special nonequilibrium conditions such as discharging, chemical vaporization, laser vaporization, or hydrocarbon pyrolysis. Consequently, they are limited in terms of yield, phase purity, crystallinity, and uniformity.<sup>2</sup> For example, the vapor–liquid–solid process, the most successful method for producing large quantities of nanowires with single-crystalline structures, requires a metal catalyst that may contaminate the nanowires and potentially change their properties.<sup>20</sup> The emerging solution-based techniques can provide high reproducibility but involve structure-directing agents mostly chosen by empirical trial and error. An interesting class is the

<sup>†</sup> Michigan State University.

<sup>‡</sup> Department of Chemistry, Northwestern University.

<sup>§</sup> Department of Physics and Astronomy, Northwestern University.

- (1) Pauzauskie, P. J.; Yang, P. *Mater. Today* **2006**, *9*, 36–45. Li, Y.; Qian, F.; Xiang, J.; Lieber, C. M. *Mater. Today* **2006**, *9*, 18–27. Hu, J. T.; Odom, T. W.; Lieber, C. M. *Acc. Chem. Res.* **1999**, *32*, 435–445.
- (2) Xia, Y. N.; Yang, P. D.; Sun, Y. G.; Wu, Y. Y.; Mayers, B.; Gates, B.; Yin, Y. D.; Kim, F.; Yan, Y. Q. *Adv. Mater.* **2003**, *15*, 353–389.
- (3) Malliakas, C. D.; Kanatzidis, M. G. *J. Am. Chem. Soc.* **2006**, *128*, 6538–6539.
- (4) Hulthen, J. C.; Jirage, K. B.; Martin, C. R. *J. Am. Chem. Soc.* **1998**, *120*, 6603–6604.
- (5) Hong, B. H.; Bae, S. C.; Lee, C. W.; Jeong, S.; Kim, K. S. *Science* **2001**, *294*, 348–351.
- (6) Tian, F.; Zhu, J.; Wei, D. *J. Phys. Chem. C* **2007**, *111*, 6994–6997.
- (7) Thurn-Albrecht, T.; Schotter, J.; Kastle, C. A.; Emley, N.; Shibauchi, T.; Krusin-Elbaum, L.; Guarini, K.; Black, C. T.; Tuominen, M. T.; Russell, T. P. *Science* **2000**, *290*, 2126–2129.
- (8) Li, Y. D.; Wang, J. W.; Deng, Z. X.; Wu, Y. Y.; Sun, X. M.; Yu, D. P.; Yang, P. D. *J. Am. Chem. Soc.* **2001**, *123*, 9904–9905.
- (9) Wu, J. J.; Liu, S. C.; Wu, C. T.; Chen, K. H.; Chen, L. C. *Appl. Phys. Lett.* **2002**, *81*, 1312–1314.
- (10) Nakamura, H.; Matsui, Y. *J. Am. Chem. Soc.* **1995**, *117*, 2651–2652.
- (11) Hoyer, P. *Langmuir* **1996**, *12*, 1411–1413.

- (12) Spahr, M. E.; Bitterli, P.; Nesper, R.; Muller, M.; Krumeich, F.; Nissen, H. U. *Angew. Chem., Int. Ed.* **1998**, *37*, 1263–1265.
- (13) Remskar, M. *Adv. Mater.* **2004**, *16*, 1497–1504. Tenne, R. *Angew. Chem., Int. Ed.* **2003**, *42*, 5124–5132.
- (14) Brorson, M.; Hansen, T. W.; Jacobsen, C. J. H. *J. Am. Chem. Soc.* **2002**, *124*, 11582–11583.
- (15) Cademartiri, L.; Malakooti, R.; O'Brien, P. G.; Migliori, A.; Petrov, S.; Kherani, N. P.; Ozin, G. A. *Angew. Chem., Int. Ed.* **2008**, *47*, 3814–3817.
- (16) Chopra, N. G.; Luyken, R. J.; Cherrey, K.; Crespi, V. H.; Cohen, M. L.; Louie, S. G.; Zettl, A. *Science* **1995**, *269*, 966–967.
- (17) Li, H. W.; Chin, A. H.; Sunkara, M. K. *Adv. Mater.* **2006**, *18*, 216–220.
- (18) Ma, R.; Bando, Y. *Chem. Mater.* **2002**, *14*, 4403–4407.
- (19) Yang, W.; Araki, H.; Hu, Q. L.; Ishikawa, N.; Suzuki, H.; Noda, T. *J. Cryst. Growth* **2004**, *264*, 278–283.
- (20) Law, M.; Goldberger, J.; Yang, P. D. *Annu. Rev. Mater. Res.* **2004**, *34*, 83–122.

series of compounds  $\text{LiMo}_3\text{Se}_3$ ,<sup>21</sup>  $\text{KMPS}_4$  ( $M = \text{Ni}, \text{Pd}$ ),<sup>22</sup> and  $\text{NaNb}_2\text{PS}_{10}$ ,<sup>23</sup> which possess quasi-1D anionic chains of  $[\text{Mo}_3\text{Se}_3]^-$ ,  $[\text{MPS}_4]^-$ , and  $[\text{Nb}_2\text{PS}_{10}]^-$ , respectively, isolated by alkali metal counteranions. These materials are synthesized as bulk crystals, however, and form nanowires and/or nanotubes only when dissolved in polar organic solvents such as *N*-methylformamide (NMF) and dimethyl sulfoxide, where their crystal lattices disassemble into structurally and electronically identical molecular wires.

Most of the known 1D nanostructures are simple atomic or binary phases. More complex multinary inorganic solids in this class are still rare, yet such materials can exhibit important properties, such as superconductivity,<sup>24</sup> giant magnetoresistance,<sup>25</sup> ferroelectricity,<sup>26</sup> liquid crystallinity,<sup>27</sup> and optical nonlinearity.<sup>28</sup> We note that polar nanowires are rare. Recently, we showed that low-dimensional chalcogenides with polar structures, such as  $\text{K}_2\text{P}_2\text{Se}_6$ ,<sup>29</sup>  $\text{LiAsS}_2$ <sup>30</sup> and  $\text{CsZrPSe}_6$ ,<sup>31</sup> can give rise to strong nonlinear optical responses and are promising in meeting technological needs in the IR and near-IR regions of the spectrum.

Here we describe the new compound  $\text{Cs}_5\text{BiP}_4\text{Se}_{12}$ , which intrinsically grows as nanowires and is obtained using a simple synthetic method. The compound is a semiconductor and shows a wide optical-transparency range through the mid- and near-IR regions as well as a strong second harmonic generation (SHG) response at  $1\ \mu\text{m}$ . Integrated photonic networks with high wavelength-conversion efficiencies in the IR region (especially at  $1.3\text{--}1.5\ \mu\text{m}$ ) are used in the broadband Internet communications industry.<sup>32</sup> Materials with a large nonlinearity and index of refraction are desirable for fiber-optic- and

nanowaveguide-based applications.<sup>33</sup> In this regard,  $\text{Cs}_5\text{BiP}_4\text{Se}_{12}$ , which is soluble in polar solvents and presumably processable, is a potential candidate. The rather surprising finding is that the repeating unit giving rise to the nanofibers is just the simple octahedral coordination complex  $[\text{Bi}(\text{P}_2\text{Se}_6)_2]^{5-}$ . The driving force for the 1D morphology is the directional association of these complexes at a supramolecular level via weak  $\text{Se}\cdots\text{Se}$  interactions and Coulomb interactions with  $\text{Cs}^+$  counteranions. Ab initio density functional theory calculations using the full-potential linearized augmented plane wave (FLAPW) method<sup>34</sup> confirm the experimental band gap and also explain the nanowire nature of  $\text{Cs}_5\text{BiP}_4\text{Se}_{12}$ . To the best of our knowledge,  $\text{Cs}_5\text{BiP}_4\text{Se}_{12}$  presents a rare example of a polar nanowire.

## 2. Experimental Section

**2.1. Reagents.** The reagents employed in this work were used as obtained: Cs metal, analytical reagent, Johnson Matthey/AESAR Group, Seabrook, NH; red phosphorus powder,  $-100$  mesh, Morton Thiokol, Inc., Danvers, MA; Se, 99.9999%, Noranda Advanced Materials, Quebec, Canada; *N,N*-dimethylformamide (DMF), ACS reagent grade, Mallinckrodt Baker Inc., Paris, KY; diethyl ether, ACS reagent grade, anhydrous, Columbus Chemical Industries, Columbus, WI. The  $\text{Cs}_2\text{Se}$  starting material was prepared by reacting stoichiometric amounts of the elements in liquid ammonia under  $\text{N}_2$ .

**2.2. Synthesis.** The synthesis of pure  $\text{Cs}_5\text{BiP}_4\text{Se}_{12}$  micro/nanofibers was achieved by reacting a  $2.5:1:4:9:5$   $\text{Cs}_2\text{Se}/\text{Bi}/\text{P}/\text{Se}$  mixture under vacuum in a fused-silica tube at  $850\ ^\circ\text{C}$  for 5 days followed by washing with degassed DMF under a  $\text{N}_2$  atmosphere ( $\sim 80\%$  yield based on Bi). Alternatively, the title compound could be obtained by reacting a stoichiometric mixture of the same reagents in a fused-silica tube at  $850\ ^\circ\text{C}$  for 3 h. Stoichiometric mixtures with shorter reaction times typically produced tiny needles instead of micro/nanofibers. Energy dispersive spectroscopy (EDS) analysis showed average compositions “ $\text{Cs}_{4.9}\text{BiP}_{3.8}\text{Se}_{11.6}$ ” and “ $\text{Cs}_{4.8}\text{BiP}_{3.9}\text{Se}_{11.8}$ ” for the respective synthetic conditions. The single crystals are stable in DMF, alcohol, and air for up to two weeks. They are soluble in NMF to give deep-orange solutions. As-prepared  $\text{Cs}_5\text{BiP}_4\text{Se}_{12}$  micro/nanowires were dispersed in EtOH and immediately formed an orange colloidal solution upon shaking a couple of times. For transmission electron microscopy (TEM) studies, the resulting suspension was diluted, sonicated, centrifuged at 4000 rpm for 1 h, and filtered by a  $0.2\ \mu\text{m}$  syringe filter to obtain evenly dispersed fibers rather than aggregated ones.

**2.3. Physical Measurements.** **2.3.1. Powder X-ray Diffraction.** Phase-purity X-ray diffraction analyses were performed using a calibrated CPS 120 INEL powder X-ray diffractometer (Cu  $K\alpha$  graphite monochromatized radiation) operating at 40 kV and 20 mA and equipped with a position-sensitive detector with a flat sample geometry.

**2.3.2. Scanning Electron Microscopy.** Scanning electron microscopy (SEM) semiquantitative analyses and morphology images of the compounds were obtained with a JEOL JSM-35C scanning electron microscope (SEM) equipped with a Tracor Northern EDS detector.

**2.3.3. Transmission Electron Microscopy.** TEM samples were diluted with ethanol and irradiated by ultrasonication. TEM and high-resolution TEM (HRTEM) images were obtained with JEOL JEM 2200 FS field-emission transmission electron microscope.

**2.3.4. Solid-State UV–Vis Spectroscopy.** Optical diffuse reflectance measurements were performed at room temperature using a Shimadzu UV-3101 PC double-beam, double-monochromator spectrophotometer operating in the  $200\text{--}2500\ \text{nm}$  region. The

- (21) Song, J. H.; Messer, B.; Wu, Y. Y.; Kind, H.; Yang, P. D. *J. Am. Chem. Soc.* **2001**, *123*, 9714–9715. Venkataraman, L.; Lieber, C. M. *Phys. Rev. Lett.* **1999**, *83*, 5334–5337. Davidson, P.; Gabriel, J. C.; Levelut, A. M.; Batail, P. *Europhys. Lett.* **1993**, *21*, 317–322. Tarascon, J. M.; Disalvo, F. J.; Chen, C. H.; Carroll, P. J.; Walsh, M.; Rupp, L. J. *Solid State Chem.* **1985**, *58*, 290–300.
- (22) Sayettat, J.; Bull, L. M.; Gabriel, J. C. P.; Jobic, S.; Camerel, F.; Marie, A. M.; Fourmigue, M.; Batail, P.; Brec, R.; Inglebert, R. L. *Angew. Chem., Int. Ed.* **1998**, *37*, 1711–1714.
- (23) Camerel, F.; Gabriel, J. C. P.; Batail, P.; Davidson, P.; Lemaire, B.; Schmutz, M.; Guilk-Krzywicki, T.; Bourgaux, C. *Nano Lett.* **2002**, *2*, 403–407.
- (24) Cava, R. J. *Science* **1990**, *247*, 656–662. Sleight, A. W. *Science* **1988**, *242*, 1519–1527.
- (25) Jin, S.; Tiefel, T. H.; McCormack, M.; Fastnacht, R. A.; Ramesh, R.; Chen, L. H. *Science* **1994**, *264*, 413–415. Moritomo, Y.; Asamitsu, A.; Kuwahara, H.; Tokura, Y. *Nature* **1996**, *380*, 141–144.
- (26) Scott, J. F.; Araujo, C. A. *Science* **1989**, *246*, 1400–1405. Dearaujo, C. A. P.; Cuchiaro, J. D.; Mcmillan, L. D.; Scott, M. C.; Scott, J. F. *Nature* **1995**, *374*, 627–629. Hemberger, J.; Lunkenheimer, P.; Fichtl, R.; von Nidda, H. A. K.; Tsurkan, V.; Loidl, A. *Nature* **2005**, *434*, 364–367.
- (27) Gabriel, J. C. P.; Camerel, F.; Lemaire, B. J.; Desvaux, H.; Davidson, P.; Batail, P. *Nature* **2001**, *413*, 504–508. Miyamoto, N.; Nakato, T. *Adv. Mater.* **2002**, *14*, 1267–1270. Michot, L. J.; Bihannic, I.; Maddi, S.; Funari, S. S.; Baravian, C.; Levitz, P.; Davidson, P. *Proc. Natl. Acad. Sci. U.S.A.* **2006**, *103*, 16101–16104. Miyamoto, N.; Yamada, Y.; Koizumi, S.; Nakato, T. *Angew. Chem., Int. Ed.* **2007**, *46*, 4123–4127.
- (28) Bordui, P. F.; Fejer, M. M. *Annu. Rev. Mater. Sci.* **1993**, *23*, 321–379.
- (29) Chung, I.; Malliakas, C. D.; Jang, J. I.; Canlas, C. G.; Weliky, D. P.; Kanatzidis, M. G. *J. Am. Chem. Soc.* **2007**, *129*, 14996–15006.
- (30) Bera, T. K.; Song, J.-H.; Freeman, A. J.; Jang, J. I.; Ketterson, J. B.; Kanatzidis, M. G. *Angew. Chem., Int. Ed.* **2008**, *47*, 7828–7832.
- (31) Banerjee, S.; Malliakas, C. D.; Jang, J. I.; Ketterson, J. B.; Kanatzidis, M. G. *J. Am. Chem. Soc.* **2008**, *130*, 12270–12272.
- (32) Dorn, R.; Baums, D.; Kersten, P.; Regener, R. *Adv. Mater.* **1992**, *4*, 464–473. Ma, H.; Jen, A. K. Y.; Dalton, L. R. *Adv. Mater.* **2002**, *14*, 1339–1365. Yamada, H.; Shirane, M.; Chu, T.; Yokoyama, H.; Ishida, S.; Arakawa, Y. *Jpn. J. Appl. Phys., Part 1* **2005**, *44*, 6541–6545.

(33) Knight, J. C. *Nature* **2003**, *424*, 847–851.

(34) Wimmer, E.; Krakauer, H.; Weinert, M.; Freeman, A. J. *Phys. Rev. B* **1981**, *24*, 864–875.



instrument was equipped with an integrating sphere and controlled by a personal computer. BaSO<sub>4</sub> was used as a 100% reflectance standard. The sample was prepared by grinding the crystals to a powder that was spread on a compacted bed of BaSO<sub>4</sub> powder standard material. The generated reflectance-versus-wavelength data were used to estimate the band gap of the material by converting reflectance to absorption data<sup>35</sup> according to the Kubelka–Munk equation:  $\alpha/S = (1 - R)^2/(2R)$ , where  $R$  is the reflectance and  $\alpha$  and  $S$  are the absorption and scattering coefficients, respectively.

**2.3.5. Raman Spectroscopy.** Raman spectra were recorded on a Holoprobe Raman spectrograph equipped with a charge-coupled device (CCD) camera detector using 633 nm radiation from a HeNe laser for excitation and a resolution of 4 cm<sup>-1</sup>. The laser power at the sample was estimated to be ~5 mW, and the focused laser beam diameter was ~10 μm. A total of 128 scans was sufficient to obtain spectra of good quality.

**2.3.6. Infrared Spectroscopy.** FT-IR spectra were recorded on solids in a CsI or KBr matrix. The samples were ground with dry CsI or KBr into a fine powder and pressed into translucent pellets. The spectra were recorded in the far-IR (600–100 cm<sup>-1</sup>) and mid-IR (500–4000 cm<sup>-1</sup>) regions with 4 cm<sup>-1</sup> resolution using a Nicolet 740 FT-IR spectrometer equipped with a TGS/PE detector and silicon beam splitter.

**2.3.7. Differential Thermal Analysis.** Differential thermal analysis (DTA) experiments were performed on a Shimadzu DTA-50 thermal analyzer. A sample (~30 mg) of ground crystalline material was sealed in a silica ampule under vacuum. A similar ampule of equal mass filled with Al<sub>2</sub>O<sub>3</sub> was sealed and placed on the reference side of the detector. The sample was heated to 800 at 10 °C min<sup>-1</sup>, and after 1 min, it was cooled at a rate of -10 °C min<sup>-1</sup> to 50 °C. The residues of the DTA experiments were examined by powder X-ray diffraction. Reproducibility of the results was confirmed by running multiple heating/cooling cycles. The melting and crystallization points were measured at the minimum of the endothermic peak and the maximum of the exothermic peak.

**2.3.8. X-ray Crystallography.** Since Cs<sub>5</sub>BiP<sub>4</sub>Se<sub>12</sub> crystallized in the form of a very thin microwire that is a bundle of individual nanowires, it was extremely hard to find single crystals suitable for X-ray diffraction studies. Most of the single crystals studied showed substantially diffused peaks. Intensity data for Cs<sub>5</sub>BiP<sub>4</sub>Se<sub>12</sub> were collected at 293(2) K on a STOE IPDS II diffractometer with Mo Kα radiation operating at 50 kV and 40 mA with a 34 cm diameter imaging plate. Data collection at lower temperatures was not useful because the N<sub>2</sub> stream affected the very thin wire-shaped single crystal. Individual frames were collected with a 15 min exposure time and a 1.0 ω rotation. The X-AREA, X-RED, and X-SHAPE software package was used for data extraction and integration and to apply empirical and analytical absorption corrections. The SHELXTL software package was used to solve and refine the structure. The most satisfactory refinement was obtained with the polar space group *Pmc*2<sub>1</sub>. The Cs(8) atom was modeled as split into Cs(8A) and Cs(8B) sites. Their occupancy ratio was refined to 95:5. The Flack parameter  $x$  was refined to 0. The parameters for data collection and the details of the structural refinement are given in Table 1. Fractional atomic coordinates and atomic displacement parameters for the structure are listed in Table 2, and selected bond distances and angles are provided in Tables 3 and 4, respectively. All of the atoms except Cs(8) were refined to full occupancy.

**2.3.9. Electronic Band Structure Calculations.** The electronic structure calculations were performed using the highly precise

**Table 1.** Crystallographic Data and Refinement Details for Cs<sub>5</sub>BiP<sub>4</sub>Se<sub>12</sub>

formula	Cs <sub>5</sub> BiP <sub>4</sub> Se <sub>12</sub>
crystal system	orthorhombic
space group	<i>Pmc</i> 2 <sub>1</sub> (No. 26)
unit cell dimensions (Å)	$a = 7.5357(2)$ $b = 13.7783(6)$ $c = 28.0807(8)$
$Z$	4
$V$ (Å <sup>3</sup> )	2915.59(17)
$d_{\text{calc}}$ (g cm <sup>-3</sup> )	4.431
crystal dimensions (mm <sup>3</sup> )	$0.1189 \times 0.0006 \times 0.0006$
$T$ (K)	293(2)
$\lambda$ (Å)	0.71073
$\mu$ (mm <sup>-1</sup> )	27.392
$F(000)$	3304
$\theta_{\text{max}}$ (deg)	27.392
total/unique reflections	18838/6306
$R_{\text{int}}$	0.0443
no. of parameters	246
refinement method	full-matrix least-squares on $F^2$
final $R_1^a/wR_2^b$ [ $I > 2\sigma(I)$ ]	0.0626/0.1151
$R_1/wR_2$ (all data)	0.0790/0.1207
goodness of fit on $F^2$	1.077
largest diff. peak/hole (e Å <sup>-3</sup> )	2.198/−3.339

$$^a R_1 = \sum |F_o| - |F_c| / \sum |F_o|, \quad ^b wR_2 = [\sum w(F_o^2 - F_c^2)^2 / \sum w(F_o^2)]^{1/2}.$$

**Table 2.** Atomic Coordinates ( $\times 10^4$ ) and Equivalent Isotropic Parameters ( $\times 10^3$  Å<sup>2</sup>) for Cs<sub>5</sub>BiP<sub>4</sub>Se<sub>12</sub> at 293(2) K<sup>a,b</sup>

atom	$x$	$y$	$z$	$U_{\text{eq}}$
Cs(1)	5000	1495(2)	1862(1)	10(1)
Cs(2)	5000	1511(2)	85(1)	17(1)
Cs(3)	5000	1680(2)	6808(1)	22(1)
Cs(4)	5000	5132(2)	3542(1)	20(1)
Cs(5)	5000	5212(2)	1653(1)	21(1)
Cs(6)	0	1356(1)	5139(1)	9(1)
Cs(7)	0	1675(2)	3247(1)	20(1)
Cs(8A)	0	1680(2)	6780(1)	21(1)
Cs(8B)	−1080(60)	1710(20)	6823(12)	21(1)
Cs(9)	0	4953(2)	209(1)	17(1)
Cs(10)	0	7879(2)	3559(1)	22(1)
Bi(1)	5000	1681(1)	4219(1)	6(1)
Bi(2)	0	3406(1)	1777(1)	10(1)
P(1)	5000	50(7)	3042(3)	15(2)
P(2)	5000	594(6)	8775(3)	12(2)
P(3)	5000	2792(6)	5492(3)	7(1)
P(4)	5000	3750(6)	4835(3)	9(2)
P(5)	0	871(6)	1187(3)	8(2)
P(6)	0	2200(6)	737(3)	7(2)
P(7)	0	4521(7)	2829(3)	18(2)
P(8)	0	5922(7)	2417(3)	16(2)
Se(1)	2540(3)	382(2)	7718(1)	19(1)
Se(2)	5000	1658(3)	3155(1)	12(1)
Se(3)	5000	7873(3)	3753(1)	21(1)
Se(4)	2597(3)	24(2)	4122(1)	15(1)
Se(5)	2594(3)	3137(2)	5873(1)	12(1)
Se(6)	5000	1308(2)	5210(1)	9(1)
Se(7)	5000	4745(2)	36(2)	21(1)
Se(8)	2633(3)	3322(2)	4423(1)	12(1)
Se(9)	2406(3)	83(2)	1005(1)	11(1)
Se(10)	0	1339(2)	1933(1)	10(1)
Se(11)	0	1846(3)	3(1)	22(1)
Se(12)	2378(3)	3025(2)	962(1)	13(1)
Se(13)	0	4821(4)	3564(1)	29(1)
Se(14)	2390(3)	3734(2)	2576(1)	20(1)
Se(15)	2467(3)	6631(2)	2605(1)	17(1)
Se(16)	0	5509(2)	1653(1)	11(1)

<sup>a</sup> The occupancies of Cs(8A) and Cs(8B) are 95 and 5%, respectively. All other sites are fully occupied. <sup>b</sup>  $U_{\text{eq}}$  is defined as one-third of the trace of the orthogonalized  $U_{ij}$  tensor.

FLAPW method<sup>34</sup> within the density functional theory scheme. The experimentally obtained lattice parameters and atomic coordinates

(35) (a) Wendlandt, W. W.; Hecht, H. G. *Reflectance Spectroscopy*; Interscience Publishers: New York, 1966. (b) Kortüm, G. *Reflectance Spectroscopy: Principles, Methods, Applications*; Springer: Berlin, 1969. (c) Tandon, S. P.; Gupta, J. P. *Phys. Status Solidi* **1970**, *38*, 363–367. (d) Chung, D. Y.; Choi, K. S.; Iordanidis, L.; Schindler, J. L.; Brazis, P. W.; Kannewurf, C. R.; Chen, B. X.; Hu, S. Q.; Uher, C.; Kanatzidis, M. G. *Chem. Mater.* **1997**, *9*, 3060–3071. (e) Stephan, H. O.; Kanatzidis, M. G. *Inorg. Chem.* **1997**, *36*, 6050–6057.

**Table 3.** Selected Bond Distances (Å) for Cs<sub>5</sub>BiP<sub>4</sub>Se<sub>12</sub> at 293(2) K

Bi(1)–Se(2)	2.986(3)	Bi(2)–Se(10)	2.882(4)
Bi(1)–Se(4)	2.927(3) × 2	Bi(2)–Se(12)	2.953(3) × 2
Bi(1)–Se(6)	2.832(3)	Bi(2)–Se(14)	2.914(3) × 2
Bi(1)–Se(8)	2.937(3) × 2	Bi(2)–Se(16)	2.917(3)
P(1)–Se(1)	2.149(5) × 3	P(5)–Se(9)	2.175(5) × 2
P(1)–Se(2)	2.238(10)	P(5)–Se(10)	2.192(8) × 2
P(2)–Se(3)	2.114(9) × 2	P(6)–Se(11)	2.118(8)
P(2)–Se(4)	2.226(5) × 3	P(6)–Se(12)	2.214(5) × 2
P(3)–Se(5)	2.159(5) × 2	P(7)–Se(13)	2.105(10)
P(3)–Se(6)	2.193(8)	P(7)–Se(14)	2.219(7) × 2
P(4)–Se(7)	2.148(8) × 2	P(8)–Se(15)	2.165(5) × 2
P(4)–Se(8)	2.206(5) × 2	P(8)–Se(16)	2.220(9)
P(1)–P(2)	2.241(12) × 2	P(5)–P(6)	2.224(11)
P(3)–P(4)	2.268(12)	P(7)–P(8)	2.252(13)

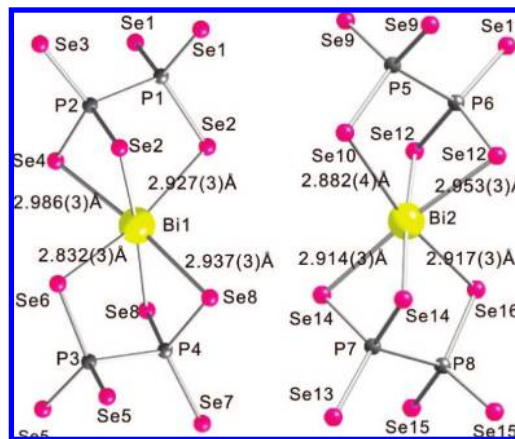
**Table 4.** Selected Bond Angles (deg) for Cs<sub>5</sub>BiP<sub>4</sub>Se<sub>12</sub> at 293(2) K<sup>a</sup>

Se(2)–Bi(1)–Se(4)	84.21(7)	P(1)#7–P(2)–Se(3)#5	111.6(4)
Se(2)–Bi(1)–Se(6)	168.91(10)	Se(10)–Bi(2)–Se(12)	86.67(7)
Se(2)–Bi(1)–Se(8)	101.78(7)	Se(10)–Bi(2)–Se(14)	92.05(8)
Se(4)–Bi(1)–Se(4)#1	76.45(10)	Se(10)–Bi(2)–Se(16)	178.10(11)
Se(4)–Bi(1)–Se(6)	87.09(7)	Se(12)–Bi(2)–Se(12)#2	74.74(10)
Se(4)–Bi(1)–Se(8)	104.06(6)	Se(12)–Bi(2)–Se(14)	104.44(6)
Se(4)#1–Bi(1)–Se(8)	174.01(7)	Se(12)–Bi(2)–Se(14)#2	178.51(9)
Se(6)–Bi(1)–Se(8)	86.98(7)	Se(12)–Bi(2)–Se(16)	94.84(8)
Se(8)–Bi(1)–Se(8)	74.79(9)	Se(14)–Bi(2)–Se(14)#2	76.36(11)
Se(1)#3–P(1)–Se(1)#4	119.2(4)	Se(14)–Bi(2)–Se(16)	86.45(8)
Se(1)#3–P(1)–Se(2)	109.5(3)	P(1)#7–P(2)–Se(4)#7	104.5(3)
Se(3)#5–P(2)–Se(4)#6	113.3(3)	P(2)#3–P(1)–Se(2)	105.2(4)
Se(4)#6–P(2)–Se(4)#7	108.9(4)	P(3)–P(4)–Se(7)#5	110.4(4)
Se(5)–P(3)–Se(5)#1	114.3(4)	P(3)–P(4)–Se(8)	105.7(3)
Se(5)–P(3)–P(6)	112.6(2)	P(4)–P(3)–Se(5)	106.0(3)
Se(7)#5–P(4)–Se(8)#1	113.3(3)	P(4)–P(3)–Se(6)	104.5(4)
Se(8)–P(4)–Se(8)#1	107.9(3)	P(5)–P(6)–Se(11)	111.3(4)
Se(9)–P(5)–Se(9)#2	113.0(4)	P(5)–P(6)–Se(12)	105.1(3)
Se(9)–P(5)–Se(10)	111.8(3)	P(6)–P(5)–Se(9)	106.1(3)
Se(11)–P(6)–Se(12)	113.3(2)	P(6)–P(5)–Se(10)	107.5(4)
Se(12)–P(6)–Se(12)#2	108.1(4)	P(7)–P(8)–Se(15)	105.2(3)
Se(13)–P(7)–Se(14)	114.2(3)	P(7)–P(8)–Se(16)	106.1(4)
Se(14)–P(7)–Se(14)#2	108.5(5)	P(8)–P(7)–Se(13)	109.6(5)
Se(15)–P(8)–Se(15)#2	118.3(4)	P(8)–P(7)–Se(14)	104.7(3)
Se(15)–P(8)–Se(16)	110.6(3)		

<sup>a</sup> Symmetry transformations used to generate equivalent atoms: (#1)  $-x + 1, y, z$ ; (#2)  $-x, y, z$ ; (#3)  $-x + 1, -y, z - 1/2$ ; (#4)  $x, -y, z - 1/2$ ; (#5)  $-x + 1, -y + 1, z + 1/2$ ; (#6)  $x, -y, z + 1/2$ ; (#7)  $-x + 1, -y, z + 1/2$ .

were employed for the calculations. The core and valence states were treated fully relativistically and scalar relativistically, respectively. The spin–orbit interaction was also included self-consistently by a second variational method.<sup>36</sup> A  $5 \times 3 \times 1$  mesh of special **k**-points was used in the irreducible Brillouin zone, and the energy cutoffs for the interstitial plane-wave basis and the star functions were 13.0 and 144.0 Ry, respectively. The muffin-tin radii of P, Se, Cs, and Bi were 1.9, 2.0, 2.7, and 2.8 bohr, respectively.

**2.3.10. Nonlinear Optical Property Measurements.** We used the frequency-tripled output of a passive–active mode-locked Nd:YAG laser with a pulse width of  $\sim 15$  ps and a repetition rate of 10 Hz to pump an optical parametric amplifier (OPA). The OPA generated vertically polarized pulses in the ranges 400–685 and 737–3156 nm. In order to determine the SHG intensity as a function of the excitation energy, we tuned the wavelength of the incident light from 1000 to 2000 nm. In this range, the spectral bandwidth of the linearly polarized light from the OPA was rather broad,  $\sim 2$  meV full width at half-maximum. However, the phase-space compression phenomena ensured effective SHG where lower-energy portions were exactly compensated by the higher-energy parts, thereby satisfying both energy and momentum conservation. The

**Figure 1.** Structure of two crystallographically independent [Bi(P<sub>2</sub>Se<sub>6</sub>)<sub>2</sub>]<sup>5−</sup> anions. Bi (yellow), P (gray), and Se (pink) atoms are labeled and selected bond distances (Å) shown.

incident laser pulse of 300  $\mu$ J was focused onto a spot 500  $\mu$ m in diameter using a 3 cm focal length lens. The corresponding incident photon flux was  $\sim 10$  GW cm<sup>−2</sup>. The SHG signal was collected from the excitation surface in the reflection geometry and focused onto a fiber-optic bundle. The output of the fiber-optic bundle was coupled to the entrance slit of a Spex Spec-One 500 M spectrometer and detected using a nitrogen-cooled CCD camera. The data collection time was 20 s. Single-crystal Cs<sub>5</sub>BiP<sub>4</sub>Se<sub>12</sub> and AgGaSe<sub>2</sub> samples were ground and separated into various size ranges using sieves. Samples were placed in capillary tubes and measured. The SHG intensity of Cs<sub>5</sub>BiP<sub>4</sub>Se<sub>12</sub> was compared with that of the benchmark material AgGaSe<sub>2</sub><sup>37</sup> in the range 500–1000 nm.

### 3. Results and Discussion

**3.1. Synthesis and Crystal Structure.** In spite of the nanowire microstructure and fibrous nature of the material, which made the selection of single crystals very challenging, we succeeded in determining the structure using single-crystal X-ray crystallography on very thin fibers. The new compound Cs<sub>5</sub>BiP<sub>4</sub>Se<sub>12</sub> adopts the polar space group *Pmc*2<sub>1</sub>. It features discrete molecular [Bi(P<sub>2</sub>Se<sub>6</sub>)<sub>2</sub>]<sup>5−</sup> anions (Figure 1), which are isolated by Cs<sup>+</sup> cations (Figure 2a). The anions are isostructural to the [In(P<sub>2</sub>Se<sub>6</sub>)<sub>2</sub>]<sup>5−</sup><sup>38</sup> and [P(P<sub>2</sub>Se<sub>6</sub>)<sub>2</sub>]<sup>5−</sup><sup>39</sup> anions. There are two crystallographically unique Bi atoms, and each octahedrally coordinated Bi<sup>3+</sup> center is capped by two chelating tridentate [P<sub>2</sub>Se<sub>6</sub>]<sup>4−</sup> units from opposite directions (Figure 1). Although the respective [Bi(P<sub>2</sub>Se<sub>6</sub>)<sub>2</sub>]<sup>5−</sup> molecules are acentric because of the distorted [BiSe<sub>6</sub>] octahedra, the polar structure arises from the noncentrosymmetric packing of Cs<sup>+</sup> ions. As expected from the polar crystal class *mm*2 of the space group *Pmc*2<sub>1</sub>, the coordination environment of the Cs atoms results in a macroscopic alignment of the dipole moments along the *c* axis (Figure 2b), resulting in the polar nature.<sup>40</sup> The absence of a mirror plane perpendicular to the 2<sub>1</sub> screw axis creates the polar structural arrangement of the compound. The Bi–Se distances are normal, ranging from 2.832(3) to 2.986(3) Å. The P–Se distances range from 2.114(9) to 2.241(12) Å. The P–P

(36) MacDonald, A. H.; Pickett, W. E.; Koelling, D. D. *J. Phys. C* **1980**, 13, 2675–2683.

(37) Nikogosyan, D. N. *Nonlinear Optical Crystals: A Complete Survey*; Springer-Science: New York, 2005.

(38) Chondroudis, K.; Chakrabarty, D.; Axtell, E. A.; Kanatzidis, M. G. *Z. Anorg. Allg. Chem.* **1998**, 624, 975–979.

(39) Chung, I.; Jang, J. I.; Gave, M. A.; Weliky, D. P.; Kanatzidis, M. G. *Chem. Commun.* **2007**, 4998–5000.

(40) Halasyamani, P. S.; Poeppelmeier, K. R. *Chem. Mater.* **1998**, 10, 2753–2769.



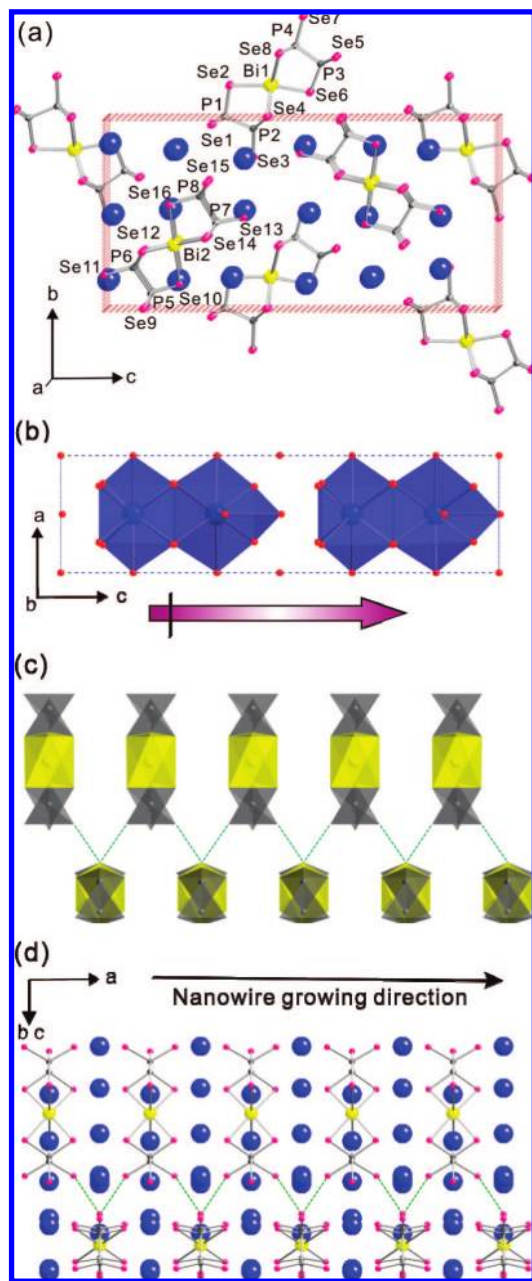


**Figure 2.** (a) Structure of  $\text{Cs}_5\text{BiP}_4\text{Se}_{12}$  viewed down the  $a$  axis (down the fiber direction). Bi (yellow), P (gray), and Se (pink) atoms are labeled. Large blue circles are Cs atoms. (b) Coordination environment of Cs atoms in a polyhedral representation showing the alignment of the macroscopic dipole moment along the  $c$  axis. (c) Polyhedral and (d) ball-and-stick representations of a pseudo-2D  $[\text{Bi}(\text{P}_2\text{Se}_6)_2]^{5-}$  chain viewed along the  $[021]$  direction. The green dashed lines depict the short nonbonding interactions  $[3.478(3) \text{ \AA}]$  between Se(5) and Se(16). In (c), light polyhedra depict  $[\text{BiSe}_6]$  octahedra and dark ones  $[\text{P}_2\text{Se}_6]^{4-}$  units; Cs atoms have been omitted.

distances of 2.224(11) to 2.252(11)  $\text{\AA}$  are typical. Noteworthy is the unusually short intermolecular  $\text{Se}(5) \cdots \text{Se}(16)$  nonbonding interaction at 3.478(3)  $\text{\AA}$ , which is much shorter than the van der Waals radii sum of 3.8  $\text{\AA}$ .<sup>41</sup> This weak interaction is important in enabling the compound to organize in an infinite pseudo-1D structure along the  $a$  axis (Figure 2c,d). However, the ionic interaction of  $\text{Cs}^+$  with  $[\text{Bi}(\text{P}_2\text{Se}_6)_2]^{5-}$  is also prominent, as we will argue later. Low-dimensional compounds such as  $\text{NbSe}_3$ ,  $\text{APSe}_6$  ( $A = \text{K}, \text{Rb}, \text{Cs}$ ),<sup>42</sup>  $\text{K}_2\text{P}_2\text{Se}_6$ ,<sup>29</sup> and molecular

$\text{Rb}_4\text{P}_6\text{Se}_{12}$ <sup>43</sup> display similarly short  $\text{Se} \cdots \text{Se}$  interactions. The dipole associated with the noncentrosymmetric structure is parallel to the  $c$  axis, which is perpendicular to the nanowire direction. Other polar nanowire systems include II–IV semiconductors such as ZnO, CdS, and CdSe and the III–V semiconductors GaAs, InP, etc. In these systems, the dipole is generally aligned along the nanowire axis.  $\text{Cs}_5\text{BiP}_4\text{Se}_{12}$  is a rare example where the dipole is perpendicular to the long axis.

By comparing polychalcophosphate flux reaction conditions that favor  $\text{Cs}_5\text{Bi}(\text{P}_2\text{Se}_6)_2$  vis-à-vis  $\text{Cs}_8\text{Bi}_4(\text{P}_2\text{Se}_6)_5$ ,<sup>44</sup> we can gain deeper insight into the evolution of the structure. The latter was synthesized in a more basic 1:1.5:2  $\text{Cs}_2\text{Se}/\text{P}_2\text{Se}_5/\text{Se}$  alkali polyselenophosphate flux at 460  $^\circ\text{C}$ , giving a remarkably complicated layered structure of  $2/\infty[\text{Bi}_4(\text{P}_2\text{Se}_6)_5]^{8-}$ . In contrast, the simpler molecular complex  $[\text{Bi}(\text{P}_2\text{Se}_6)_2]^{5-}$  in the title compound was obtained in a less basic 1:1.6:3.8  $\text{Cs}_2\text{Se}/\text{P}_2\text{Se}_5/\text{Se}$  flux at 850  $^\circ\text{C}$ . In general, less basic conditions or lower flux temperatures tend to generate longer or extended fragments.<sup>45</sup> Hence, we assume that the temperature plays a more dominant role than the higher flux basicity in stabilizing  $\text{Cs}_5\text{Bi}(\text{P}_2\text{Se}_6)_2$ . Presumably, for a given flux composition, the products formed at high reaction temperatures of 800–1000  $^\circ\text{C}$  differ from those formed at intermediate temperatures of 300–600  $^\circ\text{C}$ .

**3.2. Nanowires.** The fibrous nature of  $\text{Cs}_5\text{BiP}_4\text{Se}_{12}$  is apparent by visual inspection and in SEM images. When we examined the as-prepared product, we observed aggregates of fiber bundles. As-prepared microfibers are typically millimeters in length and submicrons to tens of nanometers in thickness (Figure 3a). The thicker fibers are bundles of thinner nanowires. Thus, in this article, we refer to the as-prepared fibers as microfibers, in that mostly they are not single-nanowire strands. The microfibers can readily be split into ever thinner fibers by physical contact. TEM images of a relatively thick single microfiber confirmed that the microfibers consist of individual nanowires with uniform thickness and alignment with an interval of 2.9 nm, which is close to the dimension of the crystallographic  $c$  axis (Figure 3b). This creates the extreme difficulty in finding single crystals suitable for X-ray diffraction studies. Most of the crystals we examined showed extensive diffuse scattering normal to the  $a^*$  axis, consistent with the nanosize dimensions of the coherence length along the  $b$  and  $c$  axes (i.e., perpendicular to the fiber). The diffuse scattering is caused by the sliding of individual nanowires and chains past each other. This observation indicates that most of the microfibers are aggregated bundles of nanowires rather than genuine microfibers with a single domain.

The  $\text{Cs}_5\text{BiP}_4\text{Se}_{12}$  microfibers can be dispersed in EtOH under a  $\text{N}_2$  atmosphere to form a colloidal suspension of nanowires. The resulting colloid was diluted, ultrasonicated, and centrifuged to obtain evenly dispersed nanowires. A representative TEM image of a nanowire is shown in Figure 3c, and the selected-area electron diffraction (SAED) pattern (Figure 3c inset) shows the crystalline nature of the nanowires. EDS analysis of the sample examined by TEM showed the Cs, Bi, P, and Se to be present in the expected ratio (Figure 3d). The distribution of

(42) Chung, I.; Do, J.; Canlas, C. G.; Weliky, D. P.; Kanatzidis, M. G. *Inorg. Chem.* **2004**, *43*, 2762–2764.

(43) (a) Chung, I.; Karst, A. L.; Weliky, D. P.; Kanatzidis, M. G. *Inorg. Chem.* **2006**, *45*, 2785–2787. (b) Kanatzidis, M. G.; Huang, S. P. *Inorg. Chem.* **1989**, *28*, 4667–4669.

(44) McCarthy, T. J.; Hogan, T.; Kannewurf, C. R.; Kanatzidis, M. G. *Chem. Mater.* **1994**, *6*, 1072–1079.

(45) Kanatzidis, M. G.; Sutorik, A. C. *Prog. Inorg. Chem.* **1995**, *43*, 151–265.

(41) Bondi, A. J. *Phys. Chem.* **1964**, *68*, 441–451.

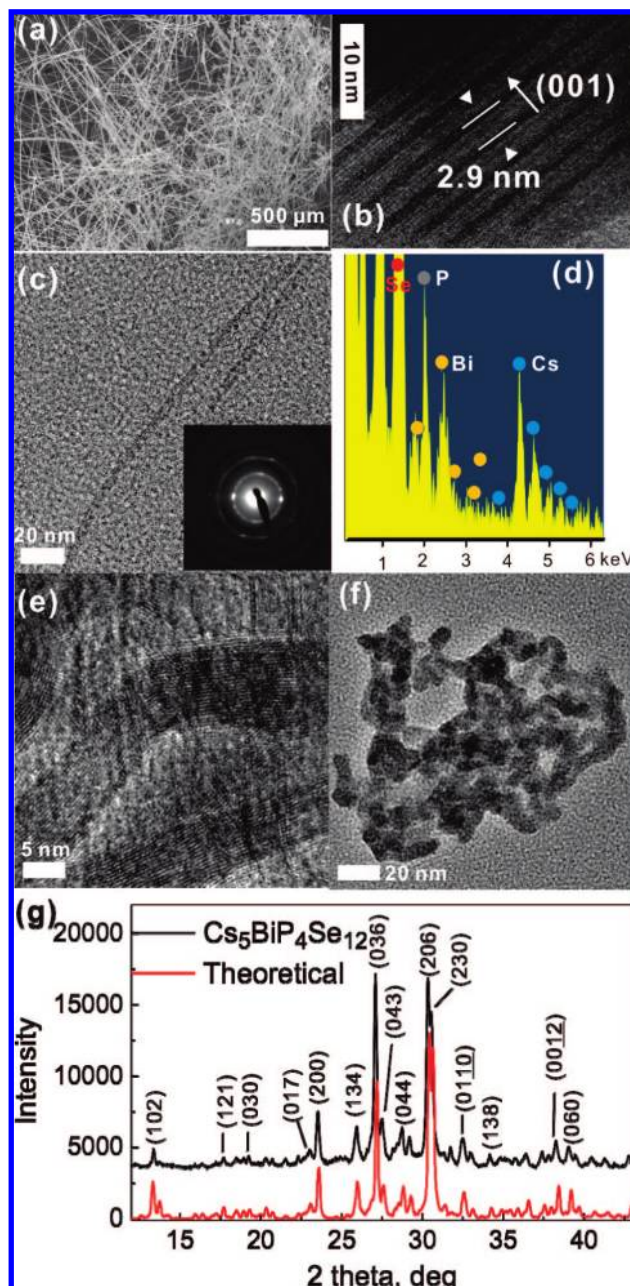


**Figure 3.** (a) Representative SEM image of  $\text{Cs}_5\text{BiP}_4\text{Se}_{12}$  microfibers, demonstrating their flexible texture. (b) TEM image of a bundle of individual nanowires, showing their uniform alignment. The lateral spacing between nanowires was measured to be 2.9 nm, which is close to the crystallographic  $c$  axis of 2.808 nm. (c) TEM image and (inset) SAED pattern of a nanowire. (d) EDS analysis of nanowires (Cs, blue; Bi, orange; P, gray; Se, red). (e) HRTEM image of individual  $\text{Cs}_5\text{BiP}_4\text{Se}_{12}$  nanowires dispersed in EtOH. (f) Tangled texture of a  $\text{Cs}_5\text{BiP}_4\text{Se}_{12}$  nanowire, depicting its striking flexibility. (g) (top) Powder X-ray diffraction pattern of a dried  $\text{Cs}_5\text{BiP}_4\text{Se}_{12}$  colloidal suspension and (bottom) the theoretical calculation. Major peaks are indexed.

nanowire diameters is  $\sim 3\text{--}9$  nm (for a single nanowire,  $d \approx 2.8$  nm). Typical long  $\text{Cs}_5\text{BiP}_4\text{Se}_{12}$  nanowires showed a striking flexibility and tangled texture (Figure 3e,f), which is extraordinary considering the single-crystalline nature of the fibers. The flexible character likely arises from the weak intra- and interchain interactions created by the short nonbonding  $\text{Se}\cdots\text{Se}$  contacts between  $[\text{Bi}(\text{P}_2\text{Se}_6)_2]^{5-}$  anions, which allow the nanowires to slide past one another and bend. These weak interactions

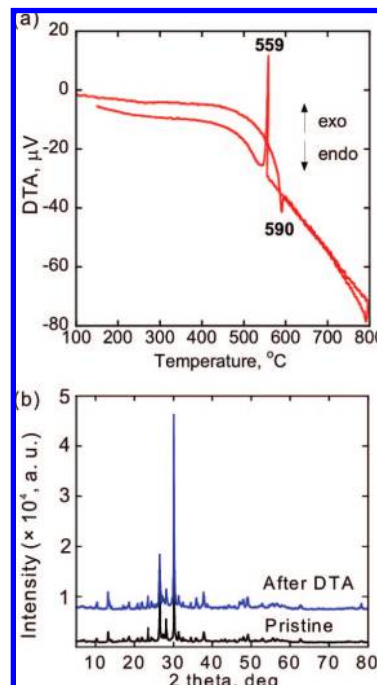


**Figure 4.** (a) DTA curve and (b) X-ray powder diffraction patterns of the pristine material and the sample obtained after DTA.

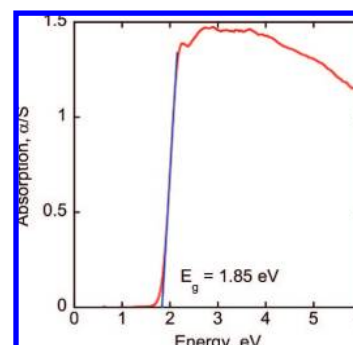


**Figure 5.** Solid-state optical absorption spectrum of  $\text{Cs}_5\text{BiP}_4\text{Se}_{12}$ .

must have a bonding character and play a key role in determining the emergent fiber behavior in this material, which arises from the packing of simple coordinating complexes of  $[\text{Bi}(\text{P}_2\text{Se}_6)_2]^{5-}$ . To confirm the phase identity of the nanowires imaged by TEM, the colloidal suspension was drop-cast, dried, and examined by powder X-ray diffraction. The patterns taken matched those of the theoretical simulation based on the single-crystal structure refinement and were fully indexed (Figure 3g), confirming that no phase degradation occurred during the dispersion process. The chemical composition obtained by EDS analysis was close to  $\text{Cs}_5\text{BiP}_4\text{Se}_{12}$ .

DTA of  $\text{Cs}_5\text{BiP}_4\text{Se}_{12}$  at a rate of  $10\text{ }^\circ\text{C min}^{-1}$  showed melting at  $590\text{ }^\circ\text{C}$  upon heating and crystallization at  $559\text{ }^\circ\text{C}$  upon cooling (Figure 4a). The powder X-ray diffraction patterns before and after melting/recrystallization were identical (Figure 4b), indicating congruent melting. The solid-state optical absorption spectrum (Figure 5) revealed a sharp absorption edge and a band gap of 1.85 eV, which is in good agreement with its dark-red color. The nearly vertical rise of the absorption coefficient suggests a direct band gap material. The nature of this gap is discussed below in conjunction with the electronic



structure calculations. In comparison, the extended polymeric  $\text{Cs}_5\text{Bi}_4(\text{P}_2\text{Se}_6)_5$  compound shows a sharp optical gap at 1.44 eV.<sup>44</sup>

**3.3. Electronic Structure Calculations.** To better understand the experimental findings, and in particular to explore the origin and nature of the band gap results, the electronic structure was calculated using the FLAPW method with the screened-exchange local density approximation (sX-LDA) and Hedin–Lundqvist<sup>46</sup> (LDA) forms of the exchange–correlation potential. The sX-LDA method has been successfully applied to a wide range of semiconductors and shows a great improvement in the excited electronic states in terms of correctly determining the band gap and band dispersion.<sup>47</sup> While the LDA calculations yield band gaps ( $E_g$ ) of 1.48 eV without spin–orbit coupling (SOC) and 1.15 eV with SOC included, the electronic structure calculated using the sX-LDA method with SOC predicts the band gap to be 2.0 eV, which is close to the experimental value of 1.85 eV. The valence band maximum (VBM) and the conduction band minimum (CBM) occur along the T–Y direction and give rise to an indirect band gap. However, the almost plateaulike narrow band dispersion ( $\leq 5$  meV) along the T–Y direction causes a large joint density of states at 2.0 eV, which is responsible for the very sharp absorption edge observed experimentally (Figure 5). The narrow band dispersions (e.g.,  $\leq 0.05$  eV for the valence top band along  $\Gamma$ –Z–T–Y) indicate the molecular nature of the compound. The relatively strong dispersion ( $\sim 0.24$  eV for the valence top band) along the  $\Gamma$ –X direction compared with the other directions arises from the Se $\cdots$ Se intermolecular interactions along the nanowire direction (the  $a$  axis in Figure 2a).

The angular-momentum-resolved densities of states (DOS) for the individual atoms reveal that the p–p mixing has a strong effect on the electronic structure and the energy-level ordering. The strong covalent interactions between mainly P and Se p orbitals form the lower energy levels (at  $-6$  to  $-4$  eV) in the valence band. The energy states derived from the relatively weak hybridization between the Bi and Se p orbitals are located between  $-4$  and  $-2$  eV. The dominating Se p character from  $-2$  eV to the VBM can be attributed to the lone-pair states of Se and the ionic bonding between Cs and Se. In this energy range, the p-orbital contributions of other elements are negligibly small, as shown in Figure 6d. The CBM shows strong Bi p character, which is highly affected by the SOC (Figure 6a,b). Therefore, the band gap excitation observed in the electronic spectrum of the compound, shown in Figure 5, is due to direct transitions from Se p to Bi p states.

It is unusual for discrete molecules to form nanofibers. Careful inspection of the crystal structure (Figures 2a and 7) shows that Cs atoms along the  $a$  axis (the fiber direction) have more anionic Se atoms available with which to interact; this gives stronger ionic interactions along the  $a$  axis than along the other directions. For instance, Figure 7d shows three different  $[\text{Bi}(\text{P}_2\text{Se}_6)_2]^{5-}$  anions (I, II, and III), with blue circles around atoms neighboring within  $4.7 \text{ \AA}$  of a Cs atom. Because they contain larger numbers of such neighboring atoms, molecular units I and II along the  $a$  axis have much stronger ionic interactions with the Cs than does molecular unit III in the  $b$ – $c$  plane (Figure 7d). As a result, those ionic interactions can predominantly propagate along the  $a$  axis, which in turn gives a better chance for crystal seeds to

grow more rapidly along the  $a$  axis (i.e., the apparent nanofiber growth direction).

To better understand how the discrete molecules give rise to the nanowire nature of  $\text{Cs}_5\text{BiP}_4\text{Se}_{12}$ , the binding energies of the molecular  $[\text{Bi}(\text{P}_2\text{Se}_6)_2]^{5-}$  units in each crystallographic direction were investigated with the LDA and Perdew–Burke–Ernzerhof (PBE)<sup>48</sup> generalized gradient approximation (GGA) forms of the exchange–correlation potential. We considered three different models in which the coordinates of two molecular units were taken from the original crystal structure (Figure 2a) in such a way that they have intermolecular interactions for different orientations in the  $b$ – $c$  plane (Figure 7a,b) and along the  $a$  axis (Figure 7c). For these models, the binding energies were estimated by examining the total energy as a function of the distance between the two molecular units.

The LDA calculations yielded binding energies of 1.90, 2.07, and 4.13 eV for the first, second, and third models in Figure 7, respectively, while the GGA calculations showed significantly smaller binding energies of 0.84, 0.87, and 3.35 eV, respectively. The difference between the binding energies from the LDA and the GGA comes mainly from the van der Waals interactions. While the strongest interactions are the ionic interactions between the molecular  $[\text{Bi}(\text{P}_2\text{Se}_6)_2]^{5-}$  units, there are also van der Waals closed-shell interactions, for which the LDA in general shows largely overestimated binding energies of the bonds. The GGA, in contrast, may give over- or underestimated or even no binding energies, depending on the particular GGA form [i.e., Becke–Lee–Yang–Parr (BLYP)<sup>49</sup> or PBE] employed.<sup>50</sup> Even with the deficiency of these exchange–correlation approximations for the van der Waals interactions, both the LDA and GGA showed significantly stronger bonds in the third model, which is the interaction along the fiber direction. This is, therefore, the fastest-growing direction, which is consistent with the nanofiber nature found experimentally. The electronic structure calculations on  $\text{Cs}_5\text{BiP}_4\text{Se}_{12}$  clearly demonstrate the existence of dominating interactions along specific directions.

**3.4. Spectroscopy and Nonlinear Optical Response.** The Raman spectrum of  $\text{Cs}_5\text{BiP}_4\text{Se}_{12}$  is very active, with shifts at 118, 143, 172, 221, 300, 433, and 467  $\text{cm}^{-1}$  (Figure 8a). The peak at 221  $\text{cm}^{-1}$  is unambiguously assigned to the locally  $A_{1g}$  symmetric stretching mode of the  $\text{PSe}_3$  unit (half of the  $[\text{P}_2\text{Se}_6]^{4-}$  ligand).<sup>21</sup> The peaks below 200  $\text{cm}^{-1}$  are possibly related to Bi–Se stretching excitations. The other shifts can be attributed to  $\text{PSe}_3$  stretching modes.

The far-IR spectrum shows peaks at 150, 181, 221, 300, 415, 440, and 502  $\text{cm}^{-1}$  (Figure 8b), similar to those of  $\text{KBiP}_2\text{Se}_6$ , which also includes  $[\text{P}_2\text{Se}_6]^{4-}$  anions.<sup>51</sup>  $\text{Cs}_5\text{BiP}_4\text{Se}_{12}$  is optically transparent from the far-IR through the mid-IR to below the band edge in the visible region (18.7 to 0.67  $\mu\text{m}$ ; Figure 8c), corresponding to the region above the  $[\text{P}_2\text{Se}_6]^{4-}$  stretching absorptions. Wide optical transparency is a critical property for application of nonlinear optical (NLO) materials and optical fibers in the IR region. Infrared NLO materials with high SHG response are highly desirable, for example, in telecommunications (near-IR at 1.3–1.6

(46) Hedin, L.; Lundqvist, B. I. *J. Phys. C* **1971**, 4, 2064–2083.

(47) Asahi, R.; Mannstadt, W.; Freeman, A. J. *Phys. Rev. B* **1999**, 59, 7486–7492. Bylander, D. M.; Kleinman, L. *Phys. Rev. B* **1990**, 41, 7868–7871.

(48) Perdew, J. P.; Burke, K.; Ernzerhof, M. *Phys. Rev. Lett.* **1996**, 77, 3865–3868.

(49) Becke, A. D. *J. Chem. Phys.* **1988**, 88, 2547–2553. Lee, C. T.; Yang, W. T.; Parr, R. G. *Phys. Rev. B* **1988**, 37, 785–789.

(50) Montanari, B.; Ballone, P.; Jones, R. O. *J. Chem. Phys.* **1998**, 108, 6947–6951. Wu, Q.; Yang, W. T. *J. Chem. Phys.* **2002**, 116, 515–524.

(51) Breshears, J. D.; Kanatzidis, M. G. *J. Am. Chem. Soc.* **2000**, 122, 7839–7840.

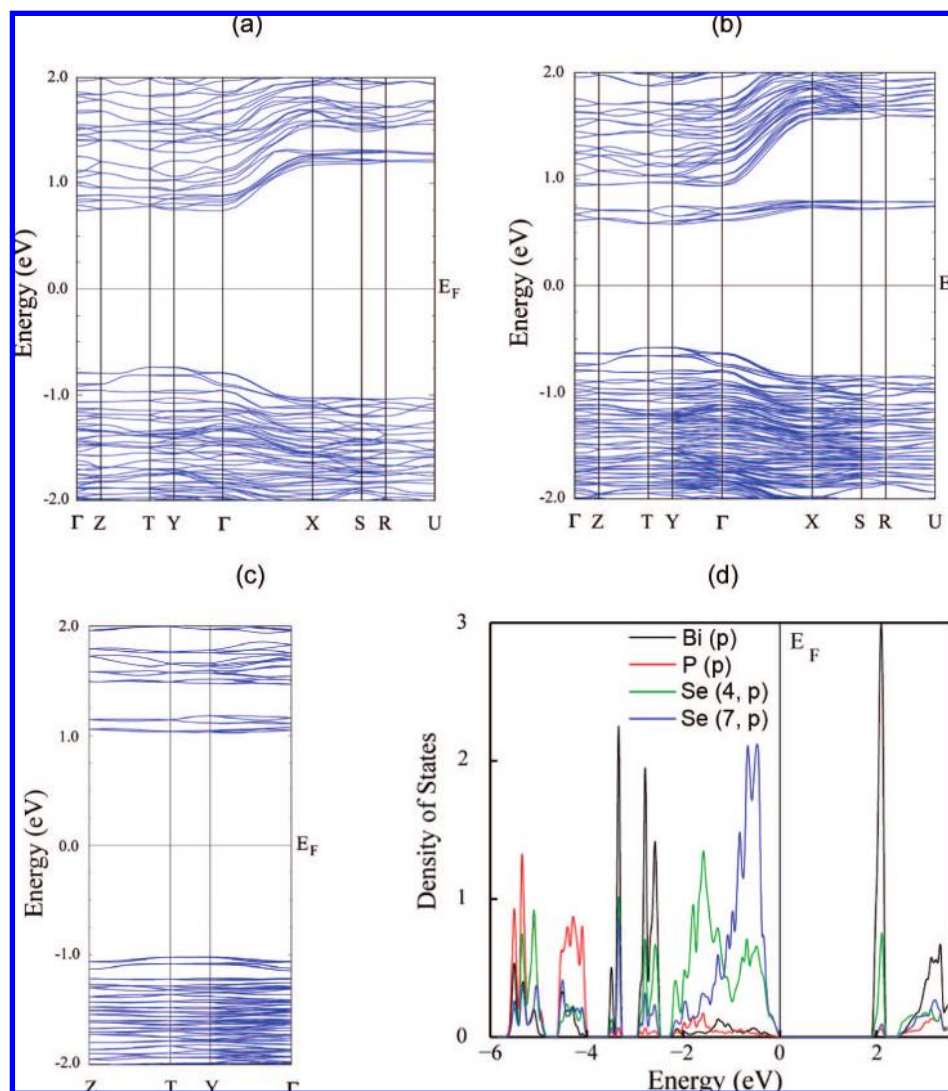


**Figure 6.** Band structures calculated using (a) LDA ( $E_g = 1.45$  eV), (b) LDA with SOC ( $E_g = 1.15$  eV), and (c) sX-LDA with SOC ( $E_g = 2.0$  eV) [in (c), results are shown for only a small part of the Brillouin zone, namely, Z–T–Y–Γ]. (d) Projected densities of states for p orbitals of the individual elements (Bi, P, Se) calculated using sX-LDA with SOC.

$\mu\text{m}$ );<sup>52</sup> sensing for organic and inorganic molecules,<sup>53</sup> including chemical-warfare agents,<sup>54</sup> biohazards,<sup>55</sup> explosives,<sup>56</sup> and pollutant detection<sup>57</sup> in the molecular fingerprint region (2–12  $\mu\text{m}$ ); and medical surgery applications (mid-IR at 10.6  $\mu\text{m}$ ).<sup>58</sup>

Because of the polar crystal structure of  $\text{Cs}_5\text{BiP}_4\text{Se}_{12}$ , we investigated its NLO properties. Using a modified Kurtz powder method,<sup>59</sup> we measured the SHG response for polycrystalline samples with sizes of 45–63  $\mu\text{m}$  using 1.2–2

$\mu\text{m}$  fundamental idler radiation from a tunable OPA. The SHG response could be observed only for wavelengths longer than 0.79  $\mu\text{m}$  because of optical absorption above the band edge. Because the SHG intensity increased with increasing wavelength up to 1  $\mu\text{m}$ , the upper limit of the tunable laser used in the SHG experiments, the SHG response of  $\text{Cs}_5\text{BiP}_4\text{Se}_{12}$  appears to be affected by optical absorption over the whole detection range (Figure 9a). Accordingly, the SHG intensities of  $\text{Cs}_5\text{BiP}_4\text{Se}_{12}$  are expected to increase continuously with increasing wavelength, reaching a plateau when the second harmonic enters the optically transparent region. The SHG intensities obtained were compared with those of  $\text{AgGaSe}_2$ , which is a representative NLO material for IR applications (Figure 9a).<sup>37</sup> All of the samples were similarly prepared with the same range of particle sizes, and identical laser settings were used. The SHG intensity of  $\text{Cs}_5\text{BiP}_4\text{Se}_{12}$  is  $\sim 2$  times larger than that of  $\text{AgGaSe}_2$  at 1  $\mu\text{m}$ , showing good performance in converting short-wave IR (Figure 9b).

(52) Islam, M. N. *Phys. Today* **1994**, 47, 34–40.

(53) Tittel, F. K.; Richter, D.; Fried, A. *Top. Appl. Phys.* **2003**, 89, 445–510.

(54) Pushkarsky, M. B.; Webber, M. E.; Macdonald, T.; Patel, C. K. N. *Appl. Phys. Lett.* **2006**, 88, 044103.

(55) Pestov, D.; Wang, X.; Ariunbold, G. O.; Murawski, R. K.; Sautenkov, V. A.; Dogariu, A.; Sokolov, A. V.; Scully, M. O. *Proc. Natl. Acad. Sci. U.S.A.* **2008**, 105, 422–427.

(56) Pushkarsky, M. B.; Dunayevskiy, I. G.; Prasanna, M.; Tsekoun, A. G.; Go, R.; Patel, C. K. N. *Proc. Natl. Acad. Sci. U.S.A.* **2006**, 103, 19630–19634.

(57) Pushkarsky, M.; Tsekoun, A.; Dunayevskiy, I. G.; Go, R.; Patel, C. K. N. *Proc. Natl. Acad. Sci. U.S.A.* **2006**, 103, 10846–10849.

(58) Jean, B.; Bende, T. *Top. Appl. Phys.* **2003**, 89, 511–544.

(59) Dougherty, J. P.; Kurtz, S. K. *J. Appl. Crystallogr.* **1976**, 9, 145–158. Kurtz, S. K.; Perry, T. T. *J. Appl. Phys.* **1968**, 39, 3798–3813.

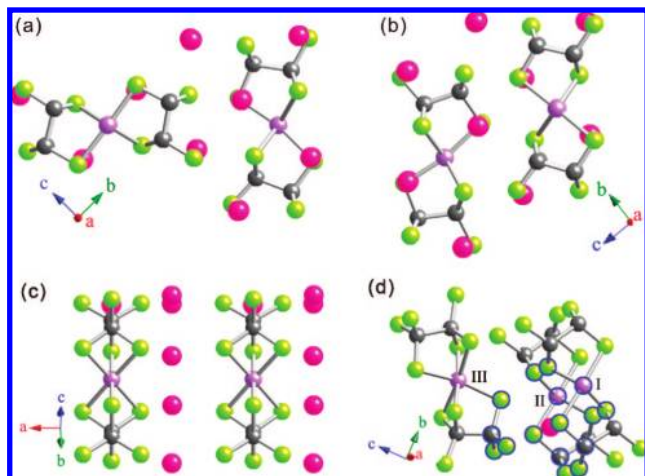


**Figure 7.** (a–c) Three different models taken from the original crystal structure (Figure 2a) for use in the binding energy calculations (see the text). In (a) and (b), the two molecular units have interactions in the  $b$ – $c$  plane, while those in (c) interact along the  $a$ -axis. (d) Three molecular  $[\text{Bi}(\text{P}_2\text{Se}_6)_2]^{5-}$  units (I, II, and III), in which atoms neighboring within 4.7 Å of the Cs atom are circled in blue. Pink, purple, gray, and green balls represent Cs, Bi, P, and Se atoms, respectively.

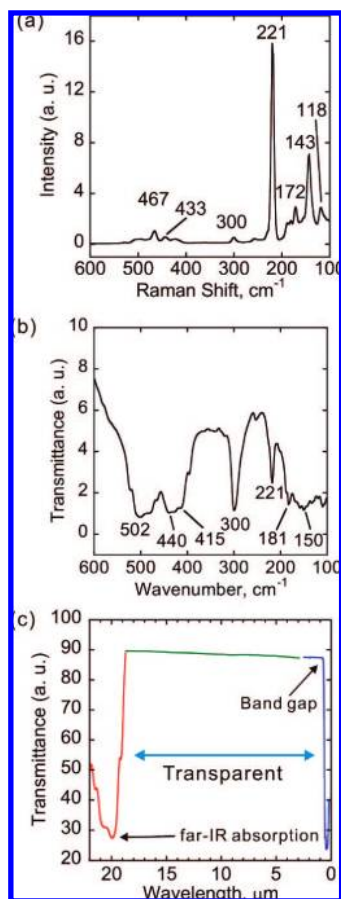


**Figure 8.** (a) Raman, (b) far-IR, and (c) far-IR/mid-IR/vis absorption spectra of  $\text{Cs}_5\text{BiP}_4\text{Se}_{12}$ . A wide transparency range of  $\text{Cs}_5\text{BiP}_4\text{Se}_{12}$  between 18.7  $\mu\text{m}$  in the far-IR region and 0.67  $\mu\text{m}$  in the visible region is shown.

The SHG intensity reached a maximum for 32–45  $\mu\text{m}$ -sized particles and decreased for larger sizes. Thus,  $\text{Cs}_5\text{BiP}_4\text{Se}_{12}$  is type-I non-phase-matchable in the spectral range we

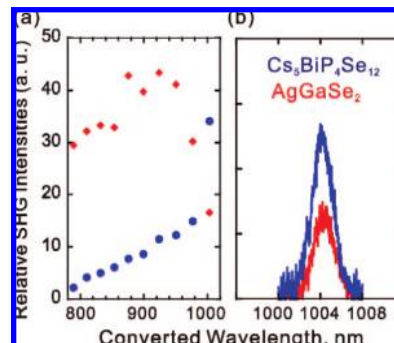


**Figure 9.** (a) Relative SHG intensities of  $\text{Cs}_5\text{BiP}_4\text{Se}_{12}$  (●) to  $\text{AgGaSe}_2$  (◆) over a wide range of wavelengths. (b) SHG responses of  $\text{Cs}_5\text{BiP}_4\text{Se}_{12}$  (blue) and  $\text{AgGaSe}_2$  (red) at 1  $\mu\text{m}$ .

examined, and the corresponding particle size of  $38.5 \pm 6.5$   $\mu\text{m}$  could be regarded as the coherence length of  $\text{Cs}_5\text{BiP}_4\text{Se}_{12}$ . Despite this, such materials can be useful through “random” quasi-phase matching.<sup>60</sup> It should be noted that a modified Kurtz powder method may not be suitable for determining SHG intensity for samples with a microwire morphology. The Kurtz powder method assumes a relationship between the SHG intensity and particle size. However, the typical diameter of as-prepared  $\text{Cs}_5\text{BiP}_4\text{Se}_{12}$  is less than 1  $\mu\text{m}$ , so the sieves used to differentiate the size distribution did not work well in this case. For this reason, the measured SHG response reported here could be underestimated. As a result, to better understand SHG in  $\text{Cs}_5\text{BiP}_4\text{Se}_{12}$ , the use of larger single-crystal samples is required.

#### 4. Concluding Remarks

The new compound  $\text{Cs}_5\text{BiP}_4\text{Se}_{12}$  naturally forms long, flexible fibers. The compound reflects the rich structural chemistry of Bi with  $[\text{P}_y\text{Q}_z]^{n-}$  chalcophosphate ligands. The packing mode of the  $[\text{Bi}(\text{P}_2\text{Se}_6)_2]^{5-}$  molecules and the weak  $\text{Se}\cdots\text{Se}$  interactions between molecules are responsible for the self-formed long, flexible nanowires, which organize into fibers. Therefore, because of this natural tendency, the  $\text{Cs}_5\text{BiP}_4\text{Se}_{12}$  nanowires can be obtained pure and in high yield without any complex chemical or physical processes. The nanowire morphology emerges from specific intermolecular secondary interactions, which could not be predicted a priori. This discovery implies that innate 1D or 2D nanostructures may be rationally approached from crystal structure considerations. This is indicated by the significant differences in binding energies along different crystallographic directions and explains how the ostensible molecular compound grows naturally into nanofibers. The result suggests the possibility of theoretical modeling and prediction of which structural species can intrinsically produce nanofibers without complex preparation processes.  $\text{Cs}_5\text{BiP}_4\text{Se}_{12}$  is widely transparent in the near- and mid-IR, over the range from 18.8 to 0.67  $\mu\text{m}$ , and it exhibits a relatively strong SHG response, which is  $\sim 2$  times larger than that of  $\text{AgGaSe}_2$  at 1  $\mu\text{m}$ . The compound is a nearly direct band gap semiconductor with a very sharp absorption edge, and it melts congruently. This material is promising for further in-depth investigations of its NLO properties.

(60) Baudrier-Raybaut, M.; Haidar, R.; Kupeczek, P.; Lemasson, P.; Rosencher, E. *Nature* **2004**, 432, 374–376.



**Acknowledgment.** Financial support from the National Science Foundation (Grants DMR-0801855, FRG-0703382, and 0306731 U.S./Ireland cooperation) and the Northwestern University Materials Research Center (under NSF Grant DMR-0520513) for J.-H.S., A.J.F., J.I.J., and J.B.K. is gratefully acknowledged.

**Supporting Information Available:** X-ray crystallographic file in CIF format. This material is available free of charge via the Internet at <http://pubs.acs.org>.

JA808242G